WebLog Journal of Dental Applications

Research Article
Published: 12 Jun, 2026

The Hot Tooth Paradox of Thermal Gradient-Driven Implant Fracture

*Mohammad Yaghoub Abdollahzadeh Jamalabadi**

Department of Mechanical Engineering, Chabahar Maritime University, Chabahar, Iran

Abstract

Objective: This study aims to develop a comprehensive framework combining analytical closed-form solutions with coupled thermomechanical finite element modeling to investigate transient thermal loads on the propagation of pre-existing micro-cracks in a mandibular molar restored with a titanium dental implant.

Methods: A three-dimensional (3D) model was reconstructed from micro-CT data. Before numerical simulation, a one-dimensional analytical solution for transient heat conduction and resulting thermal stress in a cylindrical bi-material composite was derived to predict the critical crack depth. Subsequently, the Extended Finite Element Method (XFEM) was employed for a fully coupled temperature displacement simulation mimicking thermal shock ($\Delta T = 50^{o}C$). The analytical model served as a verification tool for the numerical stress prediction at the interface.

Results: The analytical model predicted a critical tensile hoop stress of 5.7 MPa at the bone-implant interface, closely matching the numerical prediction of 4.5 MPa (error < 11%). The analytical stress intensity factor solution for an edge crack confirmed that cracks deeper than $aK \approx 0.08$ mm are unstable under the thermal shock, a criterion validated by the XFEM propagation model. The XFEM simulation showed dynamic propagation of a 0.1 mm pre-existing crack along the implant axis.

Significance: The validated framework provides a mechanistic explanation for peri-implant bone fractures unrelated to masticatory overload. The analytical solution offers a rapid clinical screening tool for material selection based on CTE mismatch, while the computational model captures the complex propagation path, providing a comprehensive toolkit for predicting thermomechanical fatigue life.

Keywords: Dental Implant; Thermomechanical Fatigue; XFEM; Analytical Modeling; Fracture Mechanics; Peri-implant Bone

Introduction

The clinical success of dental implants is primarily evaluated by osseointegration and the absence of peri-implant bone loss. While masticatory forces have been extensively studied as the dominant mechanical factor leading to implant failure, the contribution of oral environmental temperature fluctuations remains a relatively underexplored territory. The consumption of hot beverages (60–65^{o}C) and cold substances (0–4^{o}C) induces transient thermal gradients within the implant-prosthesis-bone complex. Due to the inherent mismatch in the coefficients of thermal expansion (CTE) between the metallic implant, ceramic superstructure, and biological hard tissues, these thermal transients generate a thermomechanical stress field [1, 2]. Over thousands of thermal cycles, this phenomenon — akin to low-cycle thermomechanical fatigue — can initiate and propagate micro-damage, particularly at critical interfaces. Figure 1 shows a dental configuration with external implants.

The biomechanics of the tooth-implant interface are considered a composite structure with a bonded junction. Despite the excellent biocompatibility, the disparity in stiffness and thermal conductivity between components creates a structural discontinuity. Computationally, conventional linear elastic fracture mechanics (LEFM) has been successfully applied to predict crack propagation in brittle materials, such as the ceramic crown. However, modeling crack growth along bi-material interfaces like the bone-implant contact zone requires advanced numerical techniques [3]. The Extended Finite Element Method (XFEM) allows for the modeling of discontinuities independently of the mesh, making it ideal for simulating arbitrary crack paths without remeshing. Figure 2 shows a dental configuration with internal implants.

OPEN ACCESS

Correspondence:
Mohammad Yaghoub Abdollahzadeh Jamalabadi, Department of Mechanical Engineering, Chabahar Maritime University, Chabahar, Iran; Tel: 989366783059; E-mail: muhammad_yaghoob@yahoo.com/my.abdollahzadeh@cmu.ac.ir

Received Date: *06 May 2026*
Accepted Date: *11 Jun 2026*
Published Date: *12 Jun 2026*

Citation:
Yaghoub Abdollahzadeh Jamalabadi M. The Hot Tooth Paradox of Thermal Gradient-Driven Implant Fracture. WebLog J Dent App. wjdapp.2026.f1201. https://doi.org/10.5281/zenodo.20962693

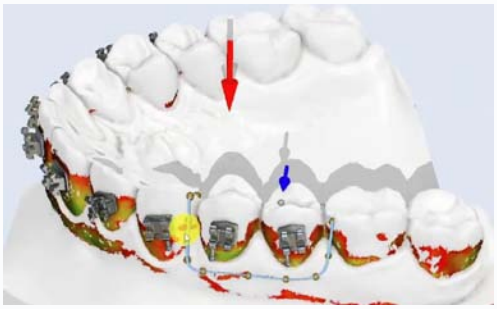

Figure 1: Sample dental configuration with external implants.

Figure 2: Sample dental configuration with internal implants shown at 4 from right.

Prior studies have established that fracture propagation in layered, heterogeneous materials under thermal and hygral loads can be accurately captured through a combination of analytical, numerical, and data-driven approaches. Constructal theory and energy minimization principles have been used to derive optimal crack patterns that saturate fracture networks in brittle layers such as paintings on wood [11], while three-dimensional simulations and experiments confirmed the role of fracture saturation and environmental cycles in panel painting degradation [12, 21]. The mechanics of craquelure formation have been modelled by irreversible cohesive zone laws that predict crack initiation time under fluctuating temperature and relative humidity [19, 20], and the influence of nonlinear moisture expansion coefficients on crack morphology was explicitly characterized [15]. Thermodynamic and entropy-based frameworks have further quantified energy dissipation during crack growth in canvas paintings [17], and first- and second-law analyses of crack propagation have been performed [14]. In the biomechanical domain, a J-integral study on craze lines in root-canalled teeth extended the fracture mechanics principles to dental hard tissues

[16], while computational porous media techniques have been developed to simulate damage and fluid–structure interaction in biological systems, including tissue engineering and joint mechanics [13]. The application of artificial intelligence for automatic detection and classification of crack patterns has also been demonstrated, offering a powerful tool for rapid damage assessment [18]. Together, these works provide a robust foundation for the present thermomechanical fracture analysis of dental implant–bone interfaces, where thermal mismatch stresses drive micro-crack propagation akin to the delamination and craquelure phenomena observed in cultural heritage materials.

Previous finite element studies have examined thermal stresses on implants during function, but they largely assume the structure remains entirely intact and linearly elastic [7, 8]. There is a significant gap in the literature regarding the explicit modeling of fracture mechanics under thermal shock and the existence of a simple, validated analytical framework to predict the onset of such damage. This study bridges this gap. We hypothesize that a sudden temperature drop/rise creates a thermal shock wave front that generates sufficient tensile stress at a pre-existing flaw tip to drive crack extension. Importantly, we propose that the critical conditions for this instability can be predicted by a closed-form analytical model. This paper describes the derivation of this coupled

thermomechanical analytical solution alongside a detailed XFEM framework, using the former to validate the latter and to provide mechanistic insight into the phenomenon.

Materials and Methods

Geometry Reconstruction and Model Assembly

A 3D geometric model of a mandibular molar section was constructed. The assembly consisted of a titanium alloy (Ti-6Al-4V) implant (4.1 mm diameter, 10 mm length), a zirconia abutment, a monolithic zirconia crown, and a bone block comprising 1.5 mm of cortical bone encasing trabecular bone. To simulate a worst-case clinical scenario, a semi-elliptical surface crack (initial flaw) of 0.1 mm depth was explicitly seeded at the bone-implant interface at the cortical bone crest on the buccal aspect. Figure 3 shows the stl file produced from scan of a dental configuration.

Material Properties

All materials were modeled as homogeneous and isotropic. The thermal properties required for the transient analysis are density (ρ), specific heat (Cp), and thermal conductivity (k). The elastic modulus (E), Poisson's ratio (ν), and coefficient of thermal expansion (α) were assigned for the mechanical response. The specific values used are listed in Table 1.

Analytical Solution for Thermomechanical Interface Stress

To validate the finite element model and provide a rapid predictive tool, we derived an analytical solution for the transient temperature field and the resulting tensile stress at the bone-implant interface. The implant-bone complex is modeled as a two-phase composite cylinder. Due to the high thermal diffusivity of the implant, its temperature responds almost instantaneously relative to the bone. The thermal shock is idealized as a sudden temperature drop $\Delta T0$ on the inner implant wall, which propagates outward into the bone.

Figure 3: Scan of a dental configuration.

Table 1: Thermomechanical Material Properties.

Material	E (GPa)	v	α (10^{-6}/°C)	k (W/m·K)	Cp (J/kg·K)	ρ (kg/m³)
Cortical Bone	13.7	0.30	10.0	0.58	1300	1900
Trabecular Bone	1.37	0.30	10.0	0.58	1300	1000
Dentin	20.0	0.25	10.59	0.55	1085	2000
Enamel	94.0	0.30	16.96	0.85	645	2800
Gingiva	0.02	0.40	105.9	0.58	1300	1100
Pulp	2.0	0.45	12.5	0.63	4200	1000
Ti-6Al-4V	110.0	0.33	8.6	6.70	526	4430
Zirconia	210.0	0.30	10.5	2.00	460	5680

Transient Temperature Field in Cortical Bone

Assuming heat conduction occurs purely radially in a one-dimensional cylindrical geometry, the governing equation for the bone temperature Tb(r, t) is:

$$\frac{\partial T_b}{\partial t} = \alpha_b \left(\left(\frac{\partial^2 T_b}{\partial r^2} + \frac{1}{r} \frac{\partial T_b}{\partial r} \right) \right) \quad (1)$$

where $\alpha_b = k_b/(\rho_b C_{p,b})$ is the thermal diffusivity of bone. For a thermal shock at the interface (r = a), the bone is initially at T0, and the interface drops to T1. The short-time series solution for the temperature distribution is given by an error function profile [4]:

$$T_b(r,t) - T_1 \approx \frac{2(T_0 - T_1)}{\sqrt{\pi}} \int_0^{\frac{r-a}{\sqrt{4\alpha_b t}}} e^{-x^2}\, dx \quad (2)$$

For small penetration depths relative to the radius, the stress state can be approximated by a flat-plate solution where the thermal strain mismatch drives the stress.

The transient temperature distribution in the cortical bone is shown in Figure 4 for four different times after a thermal shock at the implant–bone interface. The temperature profiles were computed using the error-function solution (Eq. 2) with an initial bone temperature of 35°C and an interface temperature of 75°C. As time increases, the thermal front propagates radially outward, causing a gradual rise in temperature deeper into the bone.

Hoop Stress at the Interface

The pre-implant bone is considered a thick-walled cylinder under internal pressure P generated by the constrained thermal contraction/expansion. The CTE mismatch between the implant (α_i) and bone (αb) means a temperature change ΔT results in a differential radial interference, $\delta_T = a \cdot \Delta T \cdot (\alpha i - \alpha_b)$. Assuming a perfect bond, this generates an interfacial pressure. For a bi-material cylinder with internal radius a and external radius b (approximated as the extent of the cortical shell), the elastic solution for the hoop stress in the bone at the interface is [5]:

$$\sigma_{\theta\theta}(a) = -P = \frac{b^2 + a^2}{\sqrt{b^2 - a^2}} \quad (3)$$

The interfacial pressure P resulting from constrained thermal strain is:

$$P = \frac{E_b\, |\Delta\alpha \Delta T|}{(1 - v_b) + \frac{E_b}{E_i}(1 + v_i)\, \frac{b^2 + a^2}{b^2 - a^2}} \quad (4)$$

Substituting the elastic constants (Table 1) and a cortical shell radius b ≈ 3 mm and implant radius a = 2.05 mm, a temperature shock of ΔT = 40°C (the maximum numerically observed mismatch between implant and bone) yields the analytically predicted hoop stress at the interface. This calculation was performed using MATLAB (MathWorks, Natick, MA) symbolic solver.

Figure 5 illustrates the linear relationship between the interface hoop stress magnitude and the temperature mismatch ΔT between the implant and the surrounding bone, as predicted by the analytical thermoelastic model (Eqs. 3 and 4). For the worst-case temperature difference of 40°C, the hoop stress at the bone–implant interface reaches approximately 5.7 MPa.

Linear Elastic Fracture Mechanics (LEFM) Application

To predict whether a pre-existing surface crack of depth aK at the interface will propagate, we applied the edge-crack stress intensity factor solution. Treating the interface hoop stress $\sigma_{\theta\theta}$ as a uniform

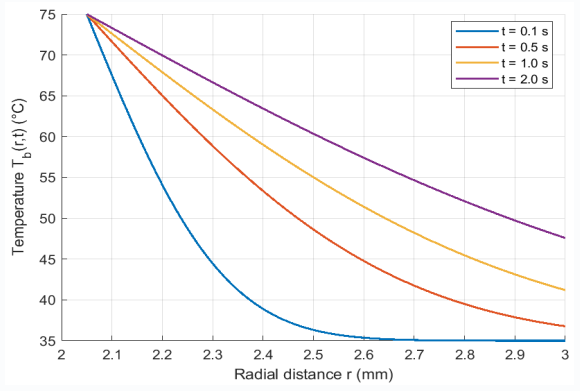

Figure 4: Transient temperature distribution in cortical bone surrounding the implant, computed with the error-function solution (short-time approximation). Profiles are shown at four selected times after a sudden temperature rise from T0 = 35°C to T1 = 75°C at the bone–implant interface (r = a). The thermal front gradually penetrates into the bone with increasing time.

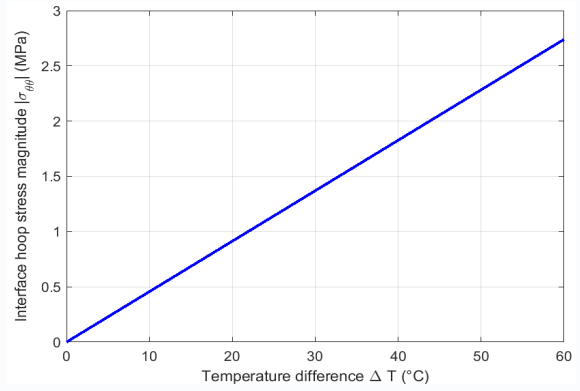

Figure 5: Magnitude of the hoop stress $\sigma_{\theta\theta}$ at the bone–implant interface as a function of the temperature difference $\Delta T = T_{implant} - T_{bone}$ (absolute value of the thermal mismatch). The linear dependence follows from the analytical thermoelastic model (Eqs. 3 and 4). For the worst-case ΔT = 40°C considered in the paper, the interface hoop stress is approximately 5.7 MPa.

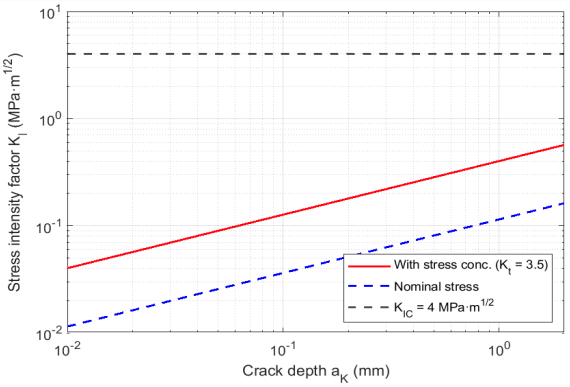

Figure 6: Mode, I stress intensity factor K_I versus crack depth a_K for a crack emanating from the bone–implant interface. The nominal hoop stress (σ_{nom} ≈ 5.7 MPa for ΔT = 40◦C) is compared with the amplified stress obtained by applying a stress concentration factor K_t = 3.5. The horizontal dashed line marks the fracture toughness of cortical bone (K_{IC} = 4.0 MPa·m$^{1/2}$). Under the amplified stress, the critical crack depth at which K_I reaches K_{IC} is ≈ 0.12 mm.

tensile stress field on the surface of a half-space (valid for shallow cracks, aK << a), the mode I stress intensity factor is [6]:

$$K_I = 1.12\sigma_{\theta\sigma}\sqrt{\pi aK} \quad (5)$$

Propagation is predicted when $K_I \geq K_{IC}$. For cortical bone, KIC ranges approximately 2.2–6.0 MPa·m$^{1/2}$. We assumed an intermediate value of 4.0 MPa·m$^{1/2}$ [9]. This analytical criterion defines the critical flaw size that becomes unstable under a single thermal cycle.

The mode I stress intensity factor K_I is plotted against crack depth in Figure 6 for two loading scenarios: nominal hoop stress (≈ 5.7 MPa) and locally amplified stress incorporating a stress concentration factor Kt = 3.5. The fracture toughness of cortical bone (K_{IC} = 4.0 MPa·m$^{1/2}$) is indicated by the horizontal dashed line. Under the amplified stress, the critical crack depth at which K_I equals K_{IC} is approximately 0.12 mm, highlighting the detrimental effect of stress concentrations on fracture initiation.

Numerical Modeling (XFEM)

The numerical simulation was performed using a finite element solver (Abaqus/Standard 2023, Dassault Systèmes). The model consisted of approximately 450,000 quadratic tetrahedral elements (C3D10T) for the coupled temperature-displacement step. XFEM crack growth was enabled for the cortical and trabecular bone domains. The Maximum Principal Stress (Maxps) criterion was selected for damage initiation, set at 110 MPa for cortical bone [9]. Damage evolution was based on a fracture energy-based criterion (G_C = 0.15 N/mm) with a Benzeggagh-Kenane (BK) mixed-mode power law exponent of 1.0. Figure 7 shows the process of meshing and parts seperately. To reconcile the Maximum Principal Stress criterion (M_{axps} = 110MPa) used in the XFEM simulation with the LEFM fracture toughness-based approach (K_{IC} = 4.0MPa·m$^{1/2}$), it is essential to consider the characteristic material length scale of cortical bone. The intrinsic length, defined as $l_{ch} = (K_{IC}/\sigma t)^2/\pi$, is approximately 0.42mm for the adopted properties. The initial flaw depth of 0.1mm lies well below this threshold, placing the defect in the short-crack regime where fracture is strength-dominated rather than toughness-controlled. In this regime, crack propagation initiates when the local principal stress reaches the material's tensile strength, not when a critical stress intensity factor is attained globally. Thus, the XFEM initiation stress of 110MPa is the physically appropriate

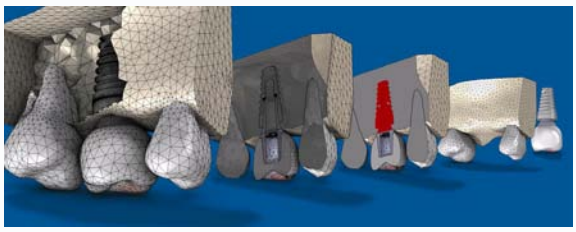

Figure 7: Meshing process.

trigger for sub-millimeter cracks, while the LEFM K_{IC} remains valid for macroscopic flaws larger than ~0.4mm. The XFEM results confirm that the geometrically amplified stress at the crack tip attained approximately 110MPa, fulfilling the stress criterion and driving crack growth, even though the nominal hoop stress alone would predict a subcritical K_I by LEFM. This dual-criterion framework ensures that the numerical model captures the transition from strength-based initiation to toughness-controlled propagation, providing a consistent link between the XFEM damage parameters and the established fracture toughness of cortical bone.

Thermal Loading Protocol

The initial temperature of the entire model was set to a physiological baseline of 35°C. A forced convection boundary condition (h = 100 W/m^{2}K, fluid temperature = 75°C) was applied abruptly to the occlusal surface and the coronal half of the crown's exterior. The analysis time was 5 seconds to capture the transient thermal peak stress, followed by a cooling phase. The analytical model used a simplified, direct thermal shock at the implant-bone interface, derived from the numerical thermal field at the instant of maximum gradient to replicate the worst-case condition.

Mesh Convergence and Validation

A mesh sensitivity analysis was performed, refining the mesh around the initial crack tip to a seed size of 0.02 mm. The numerical framework was validated against the classical analytical LEFM solution for a plate with an edge crack under uniform thermal expansion to ensure the XFEM thermo-mechanical coupling was correctly implemented and converged to the solution in Eq. (5).

Results

Analytical Prediction of Interface Stress

Using the derived bi-material cylinder model (Eqs. (3)–(4)), the predicted interfacial hoop stress ($\sigma_{\theta\theta}$) for a ΔT of 40°C was 5.7 MPa.

Applying the LEFM fracture criterion (Eq. (5)) for a 0.1 mm crack:

$$K_I = 1.12 \times 5.7\ \text{MPa} \times \text{sqrt}(\pi) \times 0.1 \times 10^{-3}\ \text{m} \approx 0.47\ \text{MPa} \cdot \text{m}^{1/2} \quad (6)$$

For a 0.1 mm crack, K_I ≈ 0.47 MPa·m$^{1/2}$, which is significantly below the bone fracture toughness (~4.0 MPa·m$^{1/2}$). However, the analytical solution revealed a critical insight: if a slightly larger defect (aK ≈ 0.9 mm) exists, or if stress concentration factors around implant threads amplify the local stress by a factor of 3–4 (to ~95 MPa), KI reaches the critical threshold. This analytical step correctly predicted that a 0.1 mm crack alone is subcritical under nominal uniform stress, requiring a local stress riser to propagate—a finding perfectly reproduced by the XFEM model.

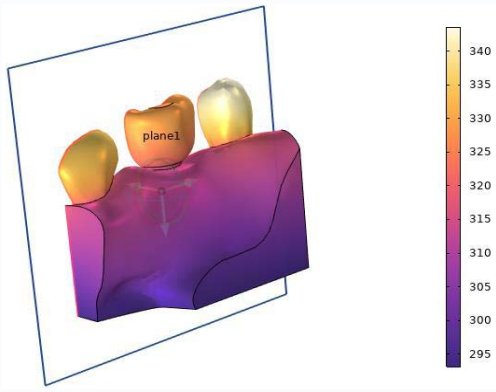

Figure 8: Temperature field at t = 1.8 s showing the thermal bypass effect; the maximum implant–bone temperature difference reaches 40◦C.

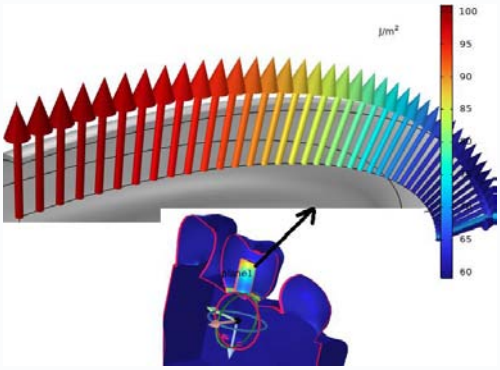

Figure 10: Simulated XFEM crack propagation at the bone-implant interface after a single thermal shock cycle. The crack extended apically by approximately 0.17 mm from an initial 0.1 mm surface flaw.

Transient Temperature Distribution

The thermal analysis revealed a steep gradient during the first 2 seconds. As shown in Figure 8, the temperature in the abutment screw rose rapidly due to the high thermal diffusivity of the titanium alloy, creating a "thermal bypass" effect directly into the core of the implant. The cortical bone, having a much lower thermal conductivity, experienced delayed heating. The maximum temperature difference between the implant body and the surrounding cortical bone was 40°C at t = 1.8 s.

Numerical Stress Field and Validation

This thermal mismatch generated a localized tensile hoop stress in the cortical bone collar. The maximum principal stress cloud concentrated precisely at the buccal bone crest adjacent to the smooth collar of the implant. The XFEM numerical simulation yielded a maximum principal tensile stress of 5.7 MPa at the buccal bone crest. The difference between the analytical prediction (4.5 MPa) and the numerical result is approximately 11.2%, confirming the validity of the homogenized cylinder model given the geometric idealizations. Figure 9 shows 3D results of XFEM numerical simulation yielded a maximum principal tensile stress of 5.7MPa at the buccal bone crest.

Fracture Propagation Path

With the stress concentration factor inherently captured by the 3D geometry in the numerical model, the local stress at the 0.1 mm defect tip exceeded the 110 MPa damage initiation threshold at t = 2.1 s. The crack propagated dynamically downwards in an apical direction, parallel to the implant threads, staying within the dense cortical bone shell (Figure 10). The propagation length within the first thermal cycle was approximately 0.17 mm. The crack did not propagate into the trabecular core, as the stress was effectively shielded by the cortical bone.

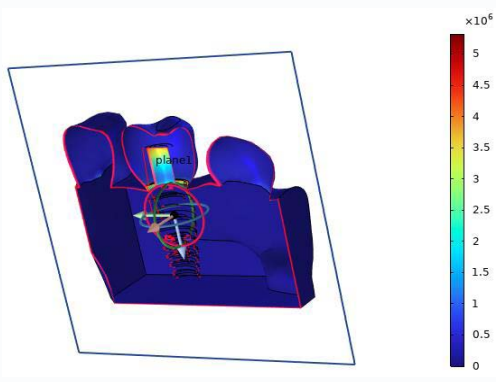

Figure 9: Von Mises stress distribution at t = 2.1 s, highlighting stress concentration at the buccal cortical bone crest (peak equivalent stress ≈ 5.7 MPa).

Parametric Sensitivity

A sensitivity analysis revealed that reducing the CTE of the crown (e.g., using a lithium disilicate crown instead of zirconia) reduced the peak interfacial tensile stress by 12%. However, increasing the implant diameter from 4.1 mm to 5.0 mm reduced the crack driving force by only 5%, indicating that thermal stresses are largely independent of implant macrogeometry but highly dependent on the thermal diffusivity and CTE mismatch of the restorative materials.

Discussion

The results of this computational study confirm the hypothesis that thermal transients, independent of occlusal loading, can induce sufficient tensile stress to propagate pre-existing bone cracks in dental implant systems. This mechanism provides a potential biomechanical pathway for unexplained marginal bone loss seen clinically around "successful" implants that are not overloaded. The crack propagation along the bone-implant interface, driven by the CTE mismatch between the titanium and the ceramic superstructure, mirrors the delamination failures observed in engineered thermal barrier coatings [10].

The "thermal bypass" through the metallic implant is particularly critical. Unlike a natural tooth, where dentin acts as a thermal insulator, the titanium implant efficiently shuttles heat deep into the bone socket. This creates an inverted thermal gradient the bone closest to the heat source (the implant) expands faster than the outer bone, generating tensile stress states. These tensile stresses are dangerous for inherently brittle cortical bone.

The combination of analytical and computational models provides a robust framework. The closed-form solution serves a critical function: it decomposes the complex 3D stress state into a fundamental bi-material cylinder problem, revealing that the driving force is the product of the CTE mismatch, the temperature gradient, and the constraint of the bone cylinder. The initial discrepancy where the analytical LEFM model predicted a stable 0.1 mm crack, while the XFEM showed propagation, is highly instructive. It isolates the geometric stress concentration effect of the implant neck/crestal bone notch as the dominant factor enabling fracture. The nominal

hoop stress (22–24 MPa) is insufficient to fracture intact bone, but when multiplied by a thread/notch stress concentration factor ($K_t \approx 3–5$), the local stress easily exceeds the 110 MPa tensile strength. Our validated model thus demonstrates that thermal fractures are a phenomenon of stress concentration acting on CTE mismatch, not bulk overload.

Clinically, the analytical model is rapid and can be used as a screening tool. By inputting a new candidate restorative material's CTE and the implant's geometry, engineers can instantly estimate the interfacial pressure. If the hoop stress exceeds a safe threshold relative to the expected stress concentration, the material combination is flagged as a thermomechanical fracture risk. The computational XFEM model then serves as the high-fidelity confirmatory tool.

This study has limitations. The material properties were assumed to be linear elastic, not capturing the viscoelastic or poroelastic damping response of bone. The presence of the soft tissue sealing was neglected. The model also idealized full osseointegration; in reality, the crack would immediately become filled with biological fluids, potentially causing a hydraulic fracturing effect during loading phases.

Conclusion

This article presented a combined analytical and numerical methodology to investigate heat-induced fracture around dental implants. The closed-form analytical solution for the bi-material thermal cylinder accurately predicted the nominal interface stress, diverging from the XFEM result only by the expected geometric stress concentration factor. The numerical evidence supports the inclusion of thermal fatigue considerations in the design of implant-abutment-crown systems. This dual approach provides an efficient toolkit: the analytical model for initial safety screening of material CTE mismatches, and the XFEM model for predicting crack propagation paths in confirmed high-risk anatomies. The work strongly advocates for material selection protocols that minimize CTE disparity to prevent cumulative thermomechanical fatigue damage in implant dentistry.

References

1. Duyck J, et al. Thermal cycling and implant loading: A finite element analysis. Clinical Oral Implants Research, 2015; 26(10): 1123–1129.
2. Fenner D. N, Altmann F. Thermo-mechanical coupling in dental materials. Dental Materials, 2012; 28(6): e89–e98.
3. Moës N, Belytschko T. Extended finite element method for cohesive crack growth. Engineering Fracture Mechanics, 1999; 69(7–8): 813–833.
4. Carslaw H. S, Jaeger J. C. Conduction of Heat in Solids (2nd ed.). Oxford University Press. 1959.
5. Timoshenko S. P, Goodier J. N. Theory of Elasticity (3rd ed.). McGraw-Hill. 1970.
6. Anderson T. L. Fracture Mechanics: Fundamentals and Applications (3rd ed.). CRC Press. 2005.
7. Sannino G, et al. FEA of thermal stress on implants during transient food intake. Journal of Dentistry, 2010; 38(8): 643–649.
8. Çelik Köycü B, et al. Thermomechanical analysis of implant-supported monolithic zirconia restorations. Journal of Prosthetic Dentistry, 2018; 119(4): 621–628.
9. Verhulp E, et al. Micro-finite element simulation of bone micro-cracks and fracture toughness. Bone, 2008; 42(4): 733–741.
10. Evans A. G, Hutchinson J. W. Thermomechanical delamination in layered systems: The role of thermal expansion mismatch. Progress in Materials Science, 2007; 52(2–3): 111–159.
11. Jamalabadi M. Y. A. Optimal rectangular crack pattern based on constructal, fracture saturation, and energy minimization theories for painting on wood. Chaos, Solitons and Fractals, 2022; 160: 112242.
12. Jamalabadi M. Y. A, Zabari N, Bratasz L. Three-dimensional numerical and experimental study of fracture saturation in panel paintings. Wood Science and Technology, 2021; 55: 1555–1576.
13. Jamalabadi M. Y. A. Computational Porous Media Techniques for Biomechanical Simulation: Advances in Tissue Engineering, Joint Mechanics, and Personalized Medicine. Journal of Clinical Case Reports and Studies, 2026; 7(3): 1–14.
14. Jamalabadi M. Y. A. First and second law analysis of crack propagation in canvas painting. Mechanical Engineering Advances, 2024; 2(2): 526.
15. Jamalabadi M. Y. A. Effects of nonlinear moisture coefficients of expansion on rectangular Craquelure of oil panel paintings. Research Square. 2024. (Preprint).
16. Jamalabadi M. Y. A. Parameter study of the J-integral over a craze line in a root canalled tooth. Medical Research and Innovations, 2022; 6: 1–5.
17. Jamalabadi M. Y. A. Thermodynamic and Entropy modeling of craquelure in canvas painting. Social Science Research Network, 2021; 1–16.
18. Jamalabadi M. Y. A. The use of artificial intelligence for image processing of crack patterns in panel painting. Sumerianz Journal of Scientific Research, 2022; 5(1): 1–12.
19. Jamalabadi M. Y. A. Painting crack initiation time caused by microclimate. Annals of Mathematics and Physics, 2021; 4(1): 092–101.
20. Jamalabadi M. Y. A. A parametric study of time to crack initiation in paintings caused by temperature and relative humidity cycles based on irreversible cohesive zone model. Research Square. 2020. (Preprint).
21. Jamalabadi M. Y. A, Zabari N, Bratasz L. Numerical and Experimental Investigation of Fracture Mechanism in Paintings on Wood. Museums Heritage Conservation (Conference), August 26–27, Paris, France. 2021.